AIAA AVIATION Forum
June 25-29, 2018, Atlanta, Georgia
2018 AIAA/CEAS Aeroacoustics Conference

10.2514/6.2018-3799

Experimental Aeroacoustic and Aerodynamic Analysis of a Large-scale Flap Side-edge Model

Daniel Acevedo-Giraldo* , Laura Botero-Bolívar.† , Lourenço T. L. Pereira.‡ and Fernando M. Catalano.§
São Carlos School of Engineering, University of São Paulo (EESC-USP), São Carlos, Brazil

Danillo C. Reis¶ and Eduardo L. C. Coelho.‖
EMBRAER, São José dos Campos, Brazil

In this research, the relationship between the parameters of a large-scale flap model and the physics responsible for flap side-edge noise generation, one of the most dominant sources of the airframe noise was investigated by performing experimental tests in a wind-tunnel. Flow-field measurements conducted with a multi-hole pitot probe located behind the flap tip were complemented by phased microphone array techniques to increase the understanding of flap side-edge noise sources and their correlations to unsteady vorticity fluctuations. Conventional beamforming and CLEAN-SC and DAMAS methodologies were used to obtain far-field acoustic spectra estimations and noise source mapping. The model used for the tests consists of an unswept isolated flap element with representative tip details presented in a medium range transport aircraft. The model instrumentation includes 106 steady pressure taps distributed chord-wise and span-wise and a trip tape that eliminates laminar boundary layer effects. Noise reduction devices were also assessed and compared to the baseline configuration regarding noise reduction. Aerodynamic and aeroacoustic tests were conducted in the LAE-1 closed circuit wind tunnel at the São Carlos School of Engineering - University of São Paulo (EESC-USP) in flow speeds up to 38 m/s. The results provided specific information about the aeroacoustic and aerodynamic characterization of the flap model dominant acoustic source mechanisms.

I. Nomenclature

α	=	Angle of attack [^{o}]
a	=	Speed of sound [m/s]
b	=	Span [m]
c	=	Chord [m]
C_p	=	Pressure coefficient [$-$]
f	=	Frequency [Hz]
M	=	Mach number ($= U/a$) [$-$]
N	=	Mach scale factor [$-$]
$OASLP$	=	Filtered Overall Sound Pressure Level [dB]
PSD	=	Power spectral density [$dB(Pa^2/Hz)$]
Re	=	Reynolds number based on the flap chord length and free-stream velocity ($=Uc/\nu$) [$-$]
St	=	Strouhal number based on the flap chord length and free-stream velocity ($=fc/U$) [$-$]
U	=	Free-stream velocity [m/s]
V^*	=	Non-dimensional velocity magnitude ($= V/U$) [$-$]
ν	=	Kinematic viscosity [m^2/s]
ω^*	=	Non-dimensional vorticity [$-$]
u^*, v^*, w^*	=	Non-dimensional cartesian component of velocity in X,Y and Z direction ($= u/U$, $= v/U$, $= w/U$)[$-$]
X, Y, Z	=	Cartesian coordinates, X positive downstream, Y positive up, Z positive to flap suction side [$-$]

*MSc student, Aeronautical Engineering Department, EESC-USP, daniel.acevedogi@usp.br.
†MSc student, Aeronautical Engineering Department, EESC-USP, laura.boterobol@usp.br.
‡MSc student, Aeronautical Engineering Department, EESC-USP, lourenco.tercio@gmail.com.
§Professor, Aeronautical Engineering Department, EESC-USP, catalano@sc.usp.br.
¶Noise and Vibration Engineer, R&T department, EMBRAER, danillo.reis@embraer.com.br.
‖Noise and Vibration Engineer, R&T department, EMBRAER, eduardo.capucho@embraer.com.br.

II. Introduction

Aircraft noise mainly refers to propulsion system noise and airframe noise [1], also known as "Non-propulsive noise of an aircraft in flight" [2]. In the 1970's aircraft noise became a subject of exhaustive research interest, after the initial studies of ultra-quiet military surveillance aircrafts in the late 1960's. Aircraft noise has increased due to the growth of aircraft operations and expansion of airport facilities close to populated areas [3]. As stated by Smith, M., (1989) [1], airframe noise is the ultimate aircraft noise barrier. In 2020 and 2025, respectively, U.S [4] and European [5, 6] governments expect to achieve aircraft noise reductions of 10 *dB* and 20 *dB* relative to the year 2000 technology.

Airframe noise research began as a consequence of noise reduction in propulsion systems resulting from the increase in the high-bypass ratio engines in 1970's, which made airframe noise a prominent component of the overall aircraft noise. From 1980 to 1990, the interest in airframe noise decreased due to the first fuel crisis. Intense airframe noise research began in the 1990's with NASA programs, such as Advance Subsonic Technology (AST) and Quiet Aircraft Technology research (QAT) [7, 8] and since then, it has been a topic of interest in aviation [9]. NASA has also developed new research programs in airframe noise under the Advanced Concepts to Test (ASCOT) and Futuristic Airframe Concepts and Technologies (FACT) Programs. All of them involve partners in both industry and academia, as NASA Langley Research Center (LaRC), to investigate and determine fundamental noise source mechanisms by relating fundamental fluid mechanics to sound generation mechanisms [7]. Many experimental, analytical, and numerical investigations have been carried out towards the understanding of the flow dynamics around aircraft and their noise sources.

Engine noise is the major contributor to the overall aircraft noise during take-off, once the engines are set to their maximum power to provide the necessary thrust. The contribution of the airframe noise is more significant during the approach operation, because the aircraft demands less thrust and the generation of engine noise is reduced. Both high-lift devices (flap and slat) and landing gear are the main sources of overall aircraft noise during approach and take-off. All of them are retracted in the cruise phase [10]. The current major detailed contributions to airframe noise for commercial aircraft are parasitic noise sources, landing gears, high-lift devices (slotted slats, flap and slat side-edges, flap and slat tracks, and spoilers) and component interaction noise sources, e.g., gear-wake/flap interaction [4, 11, 12].

The noise generated from flap side-edge and trailing-edge is recognized as one of the major noise sources of airframe noise [4, 8, 9, 13] because of two noise generation mechanisms, described by Rossignol, K., (2013) [14], The first is a direct interaction between the shear layer unsteadiness and the sharp edge, whereas the second is the induction of vortex unsteadiness interacting with the surfaces and edges. The pressure differential between the upper and lower surfaces produces an oscillating vortical system, which results in a strong broadband noise. Such a system is characterized by the generation of two separate vortices in the upstream region of the flap, i.e., one at the upper flap side contour and the other at the lower flap side contour [15]. As stated by Molin, R. and Barre, S., (2003) [16], in general, any vortical pattern in a flow generates sound as soon as its inertia has been modified, once the corresponding change in the pressure gradients also induces density fluctuations that propagate as sound. At commonly subsonic Mach numbers, sound generation occurs because convected vortical patterns interact with solid surfaces.

According to Reichenberger, J., (2016) [15] and Filippone, A., (2014) [17], flap local flow-field comprises the following noise generation mechanisms described by Rossignol, K., (2013) [14] (Fig. 1).

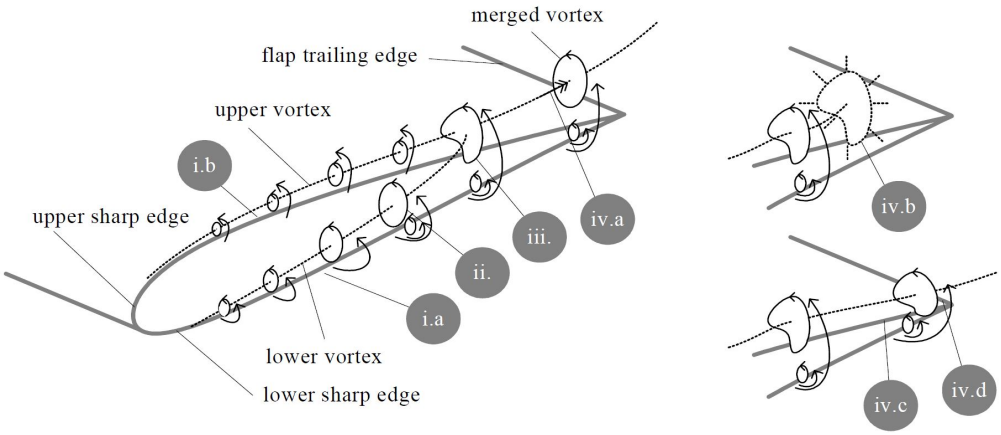

Fig. 1 Simplified scheme of the flap side-edge local flow field [18].

The flap side-edge local flow-field noise generation mechanisms are: I. Trailing-edge noise and flow separation at the tip edges. (I.a). The turbulent boundary layer on the pressure side of the flap moves across the lower flap side-edge. This mechanism is present in the entire flap chord region. (I.b). The turbulent boundary layer on the side of the flap moves across and separates at the upper flap side-edge. II. Fluctuations on the side-edge vortex pressure interacting with the flap side surface and upper side-edge. The vortex is fed by shear instabilities from lower side-edge in the mid-chord region. III. Merging of the two vortices. IV. Fluctuations in the merged vortex pressure interacting with the flap suction and the upper side-edge. (IV.a). The merged vortex moves upwards; this mechanism is limited to a small region slightly downstream of the merging location. (IV.b). The vortex breakdown is a noise source. (IV.c). The merged vortex remains close to the upper surface and interacts with the flap suction side and the upper side-edge. (IV.d). The merged vortex passes the trailing-edge and interacts with the trailing-edge corner.

A schematic representation of the spectra of flap side-edge noise and its two main contributors is provided at the bottom left corner of Fig. 2. The section cutting planes show an instantaneous photography of the vorticity field near the flap side-edge, where blue and red denote negative and positive vorticities, respectively. The vortex path is shown by the dashed line. Mid-to-high frequency vortex-edge interaction noise is detected at locations 1 and 2. The low-to-mid frequency noise production results from vortex-edge/surface interactions and is detected at locations 3 and 4.

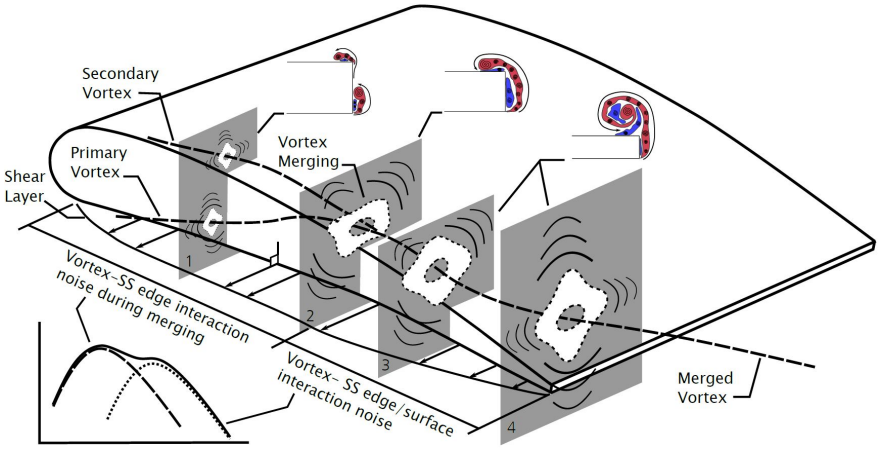

Fig. 2 Scheme of the flap side-edge local flow and vorticity field [14].

According to Drobietz, R. and Borchers, I., (2006) [18] flap side-edge noise is considered a broadband component. The post-merged vortex interacting with the flap suction side and the trailing edge; and the shear layer originating at the lower ridge of the flap tip produce most of the audible noise. The unstable merged vortex generates noise in low to mid frequencies, whereas the mid- to high-frequency noise is radiated by turbulent shear layer instabilities.

Different flow control solutions have been proposed to reduce the flap side-edge noise. The flap side-edge modifications described in the literature alter the flow-field around the flap tip by either displacing the vortex away from the flap surface, or reducing lift loading in the flap side-edge region and its strength. Although both passive control devices and active control techniques mitigate the flap side-edge noise, an aerodynamic and aeroacoustic comprehensive technological evaluation of the different real-scale devices is still a hard task.

This investigation provides a much deeper understanding of the mechanisms responsible for the flap noise generation on the subject of large-scale flap side-edge noise for the correct quantification of the noise parameters modeled in Reynolds number at take-off and landing conditions. Experimental aeroacoustic and aerodynamic measurements were conducted by a large-scale flap model, with representative tip details presented in a twin-engine short/medium range transport aircraft to provide a further step in the better understanding of the relationship between airframe noise and the phenomena of flow-field around flap side-edge. The relative contribution of each noise source to the overall airframe noise (at first with baseline flap model configuration and then the flap model with different flap side-edge geometries) is shown in the experimental measurement results of phased array microphones, static pressure taps, and flow and wake mapping. The experiments were performed in a closed wind-tunnel test section at different deflection angles and Reynolds number of approximately 1.5×10^6.

III. Test Facilities and Measurements

A. Wind Tunnel Facility

Experiments and analyses were performed in the LAE-1 wind tunnel facility at the Laboratory of Aerodynamics of the Aeronautical Engineering Department from São Carlos School of Engineering - University of São Paulo (EESC-USP). The closed circuit wind-tunnel is a low-speed facility with a closed test section of 1.3 m high, 1.7 m wide and 3.0 m long. It has an eight-blade fan, driven by a 110 hp electric motor with seven straighteners located downstream the fan, and two 54% porosity screens located before the contraction cone for turbulence reduction, which results in turbulence levels lower than 0.25%. Its maximum free flow speed is 45 m/s [19]. Figure 3 shows the plan and 3D view of the closed wind tunnel.

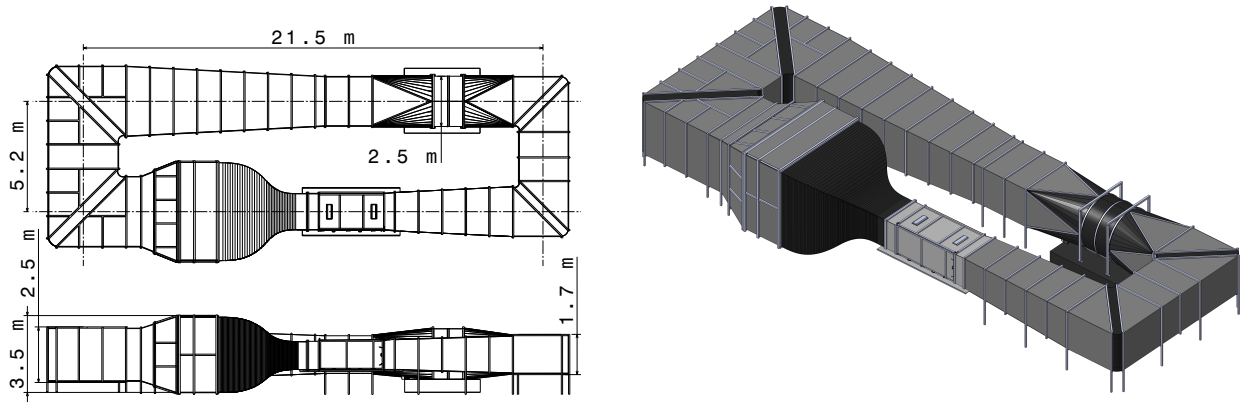

(a) LAE-1 wind tunnel plan View[20].

(b) LAE-1 wind tunnel 3D view.

Fig. 3 LAE-1 wind tunnel facility.

The LAE-1 wind-tunnel was designed originally for automotive tests, however, it has become a multi-task facility used mainly for aeronautical tests. A background noise reduction process for aeroacoustic measurements has been recently implemented due to the stringent aircraft noise regulations for aircraft certification and operations that require aeroacoustic improvements. The noise treatment processes reduced up to 5 dB of the background noise and the turbulence level decreased from the original 0.25% to 0.21%. [20].

B. Flap Model

The flap model designed for investigating the phenomena of airframe noise from side-edge was representative of a detailed flap of a conventional twin-engine short/medium range transport aircraft. A 0.7 m chord (c) flap was used for increasing both Strouhal and Reynolds number during the tests and the fidelity of results. The unswept model had also 0.7 m span (b) to match the flap side-edge and the microphone array center. The wood-aluminum model was fixed to a turn-table mounted at the wind-tunnel test section through a simplified iron body-pod formed by two spars and a circular-base (side-plate). The isolated flap model was vertically positioned in the closed test section of the wind-tunnel by only one supporting side-plate. A 12 mm length and 0.1 mm thick trip tape was used on the suction side of the flap at $x/c = 0.02$ and on its pressure side at $x/c = 0.06$ to ensure the development of fully turbulent boundary layers and avoid a premature separation of the boundary layers at the trailing-edge.

A removable flap side-edge, with the tested geometries and approximately 0.08 m span, was used at the tip of the model to facilitate the reproduction of the model details and the noise-reduction devices tested. The initial concept of flap model in the wind tunnel test section is illustrated in Fig. 4. The tests were performed for three main different configurations, i.e., baseline, which represents a common flap side-edge, the seal flap side-edge, which has real details on the flap tip and the seal flap side-edge with a tab. The last two configurations were also tested with a 22% perforated flap side-edge.

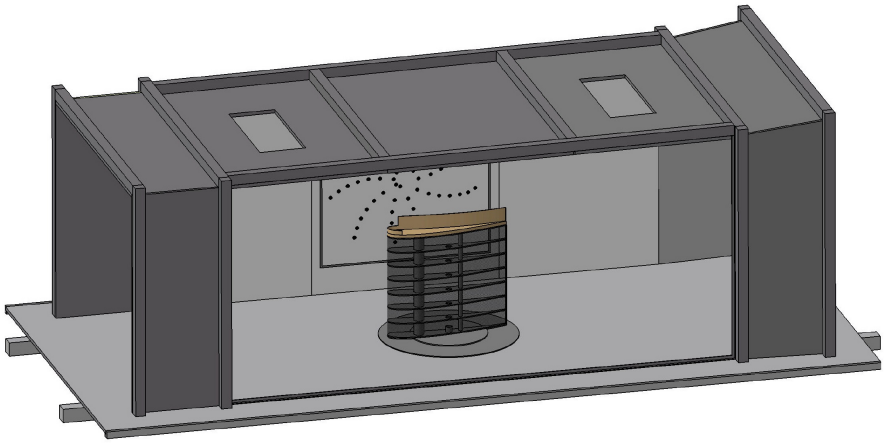

Fig. 4 Flap model view in the wind tunnel test section.

C. Test Conditions

LAE-1 wind-tunnel was operated at velocities from 26 m/s to 38 m/s and correspond to Reynolds numbers between 1.02×10^6 and 1.48×10^6, respectively. The test flow conditions were assumed at the wind tunnels location. The atmospheric conditions measured were density $\rho = 1.067\ Kg/m^3$, temperature $T = 20\ ^oC$ and pressure $P = 91.45\ KPa$. This implies a kinematic viscosity $\nu = 1.746 \times 10^{-5}\ m^2/s$, dynamic viscosity $\mu = 1.863 \times 10^{-5}\ Pa.s$ and speed of sound $a = 337\ m/s$. The flap model chord measures $c = 0.7\ m$ and Reynolds Number based on the chord length of the model is up to approximately 1.5×10^6. The flap model was tested for deflection angles $\alpha = 0^o,\ 5^o,\ 10^o,\ 15^o,\ 20^o,\ 22^o,\ 24^o,\ 26^o,\ 28^o$ and 30^o. The corresponding ranges of Mach and Reynolds numbers are given in Table 1.

Table 1 Non-dimensional flow parameters for different tests.

U [m/s]	M [-]	Re [-]
26	0.075	1.02×10^6
29	0.084	1.14×10^6
32	0.092	1.27×10^6
35	0.100	1.38×10^6
38	0.109	1.48×10^6

D. Aeroacoustic Measurements

Aeroacoustic measurements were performed in the experimental phase through phased array beamforming techniques for providing acoustic source localization and an estimation of the far-field noise spectrum.

1. Microphone Array

The measurements were taken with an array of 61 microphones flush-mounted on the test section side-wall of the wind-tunnel, facing the pressure surface of the flap model. The G.R.A.S. 46BD microphone set consists of a microphone cartridge with a pressure transducer ($40BD$) and a preamplifier ($26CB$) combination, calibrated as one unit. It provides a flat response for source localization from 4 Hz to 70 kHz ($\pm 2\ dB$) frequencies. Microphone array acquisition is performed through an IEPE PXI system composed of 4 NI PXIe-4497 boards that hold simultaneously 64 analog inputs with 24-bits resolution at maximum of 204.8 kS/s sample rate and 20 seconds of data recording. The microphone array was designed with a modified and optimized spiral geometry (Fig. 5) for measurements in a large frequency band [21]. Each microphone was calibrated by a model $NC - 74$ sound calibrator prior to noise measurements. The microphones were distributed in a 0.85 m diameter region with the flap side-edge located in the microphone array center, as shown in Fig. 6.

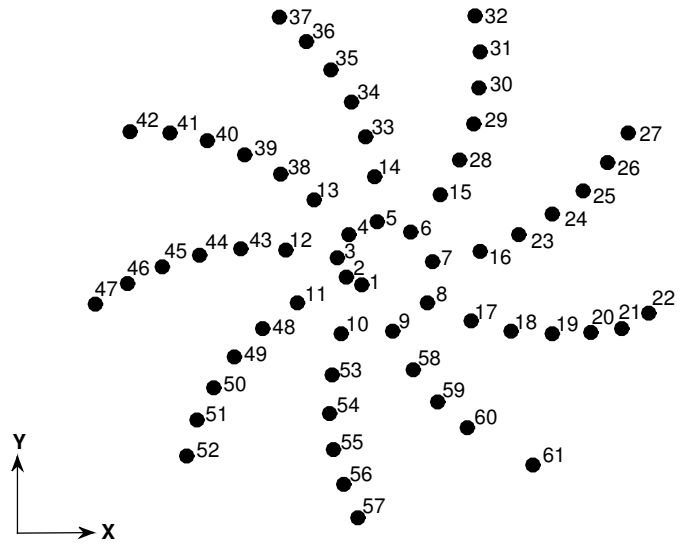

Fig. 5 Microphone array design.

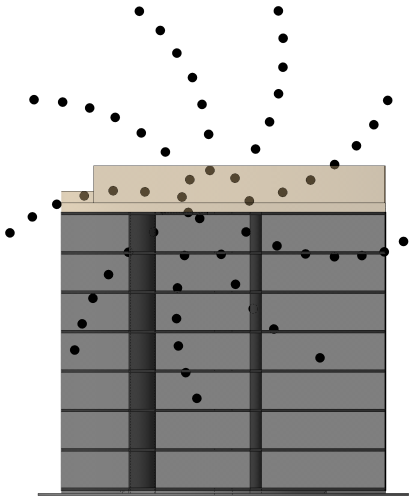

Fig. 6 Microphone array position.

E. Aerodynamic Measurements

Aerodynamic measurements demand steady experiments in the flap model. The wind tunnel was prepared for several aerodynamic tests that involved pressure distribution measurements, flow-field mapping and flow visualization techniques.

1. Free Stream Conditions

Atmospheric conditions were measured at the beginning of each test for the establishment of non-dimensional parameters and then comparisons. The atmospheric pressure was measured by a calibrated mercury barometer of 1 $mmHg$ precision and the temperature was measured inside the wind tunnel by a 0.1^o precision thermocouple. Relative humidity was measured in percentage by a 1% precision hygrometer and was used to correct the calculation of air density. The free-stream velocity was computed from the dynamic pressure measured by a pitot-static probe located at the working section wall. The probe measures both total and static pressure and is connected to a manometer, whose digital output is the difference between both pressures, which is the dynamic pressure. The precision of this instrument is 0.1 Pa and it is connected to the computer to automatically acquire data prior to each test.

2. Static Pressure Measurements

Static pressure taps were located along different model positions for the observation of the tip effects and the location of the tip vortices along the chord, observed as a local pressure difference between the flap suction and pressure sides.

The model instrumentation includes 106 steady pressure taps distributed chord-wise (57 taps along the flap chord) and span-wise (49 taps along the flap span at seven different heights) on both upper and lower sides of the flap model. Measurements were performed by a ScaniValve ZOC33/64PxX2 in the wind tunnel, which works in a ± 0.72 psi range and has 0.15% accuracy. The ScaniValve model is an extremely compact electronic pressure scanning module designed specifically for use in wind tunnels. Data are acquired by the ScaniValve connected to a local computer via FTP protocol. The procedure involves calibration of zeros and measurement of each channel of the multiplexed system.

3. Flow-Field Measurements

Flow-field measurements were taken by an L-shape 7-hole pitot probe. Such a transducer was mounted in an automatic traverse system that maps the flow behind the model, close to the flap side-edge and downstream of the trailing-edge, for obtaining the wake characteristics.

The multi-hole pitot probe is composed of a conventional cylindrical body with seven holes at its tip. The stainless steel 3.2 mm diameter probe enables high-accuracy measurements of the magnitude and direction of the flow vectors

along with static and total pressure. The acceptance angle is up to $\pm 30^o$ with an error lower than $\pm 1^o$. The velocity error is lower than $\pm 1\%$ or $\pm 1\ m/s$. The high-accuracy probe calibrations define the relationship between the probe pressures measured and the actual velocity vector sensed by the probe and the pressure transducers. To obtain correct data acquisition, pneumatic tubing was connected from the ports of the multi-hole probe to the pressure measurement system. A Dantec® three-axis traverse system was used for the probe positioning and flow mappings. Each axis movement has 0.0125 *mm* maximum accuracy and was operated by serial communication. Calibrations were performed with dedicated modules from Dantec®.

4. Flow Visualization

Flow visualizations were conducted over the flap model surface according to the oil-flow technique for the visualization of separation points, reattachment points, recirculation zones and flow direction. Oil-flow was applied for the flap tripped configuration with different side-edge tips. The entire flap model was painted black for a better visualization of the product applied.

IV. Post-Processing Analysis

A. Aeroacoustic Measurements

The post-processing analysis for aeroacoustic measurements was based on phased array microphones and beamforming techniques to map the location of the noise sources and their intensity, and generate acoustic spectrum information. Beamforming calculations were performed through Conventional beamforming [22] and CLEAN-SC methodologies [23] for all data and DAMAS [24] deconvolution methodology for selected cases.

Six Regions of Interest (ROI) were created for the beamforming integration regions (Fig. 7). The contribution measured by each part of the model and the total noise measured were studied. The ROIs were created for the total model (ROI 1), total flap side-edge (ROI 2), first flap side-edge region until 30% of the chord (ROI 3), middle flap side-edge region between 30% and 70% of the chord (ROI 4), last flap side-edge region from 70% of the chord (ROI 5), and lower part of the flap span (ROI 6). The last ROI was created for the verification of the wind-tunnel wall effect noise, which may affect results.

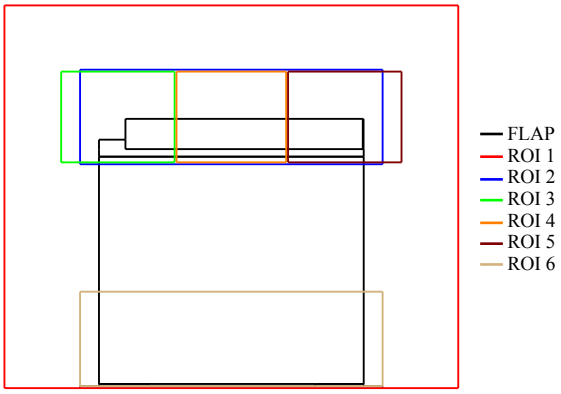

Fig. 7 Regions of interest for beamforming calculation

B. Aerodynamic Measurements

Static pressure data were obtained and used in the calculation of the pressure coefficient, a non-dimensional parameter that considers the flow over the flap model immersed in a free-stream with pressure and velocity. The reference pressure is taken at the wind tunnel test section and post-processed to produce C_p data.

Wake and flow mapping measurements were performed by a 7-hole probe and data were stored in Tecplot® data format, which enables efficient plotting and comparisons between flap side-edge geometries. The three velocity components (u,v and w) were obtained by the probe.

V. Results

A. Aerodynamic Measurement

1. Pressure Distribution

Static pressure measurements were simultaneously taken for the entire chord and span direction. Figure 8 shows the expected behavior for a pressure distribution around the flap chord of the baseline and seal flap side-edge in the closer side-edge region. The effect of the transition trip was also evaluated in terms of static pressure in the model. The comparison between the tripped and untripped cases, for several angles of attack and velocities, showed the trip device exerts a small effect on the suction peak.

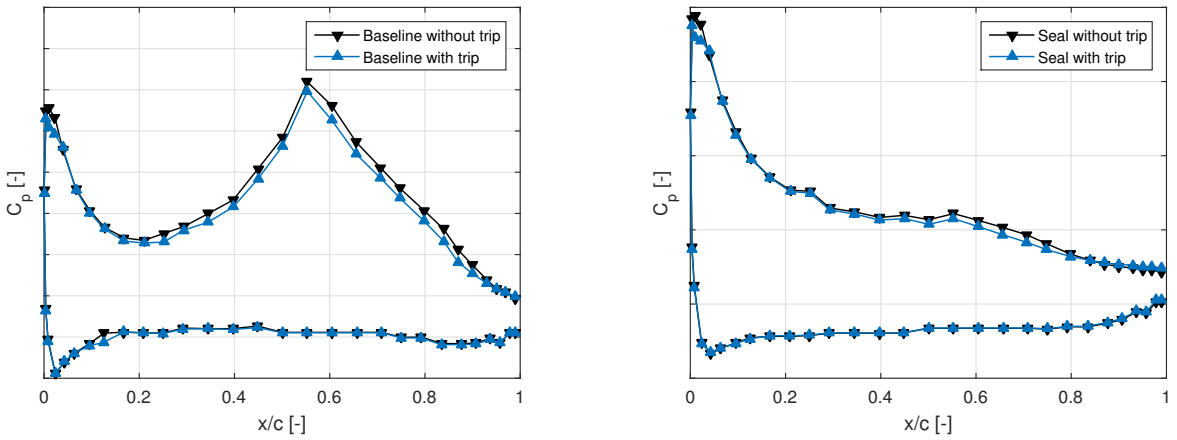

(a) Baseline flap side-edge

(b) Seal flap side-edge

Fig. 8 Pressure distribution around tripped and untripped flap model at α = 26^o and M = 0.109.

As shown in Fig. 9, the side-edge vortex in the baseline flap side-edge influences the pressure distribution in both pressure and suction side from the flap tip ($y/b = 1$) until $y/b = 0.77$, whereas the seal flap side-edge configurations move away the side-edge vortex system and increase the suction peak. The Suction peak is also affected by the vortex along the span of the model. Seal and seal with tab tips on the flap side-edge increase the span-wise uniformity.

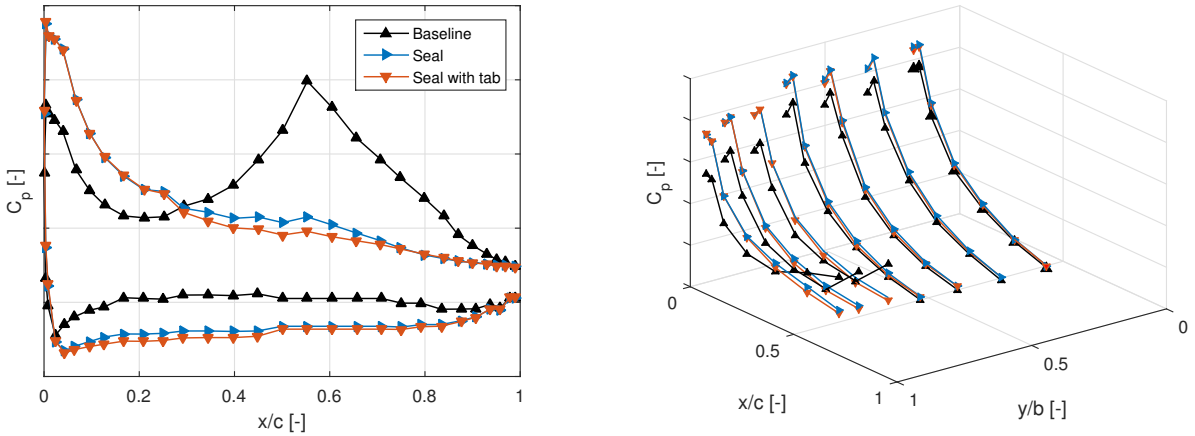

(a) Chord-wise pressure distribution

(b) Span-wise pressure distribution

Fig. 9 Comparison of pressure distribution. Span-wise taps were located on the suction side from x/c = 0.02 to x/c = 0.65 and for y/b = 0.95, 0.88, 0.77, 0.65, 0.51, 0.35 and 0.18 at α = 26^o and M = 0.109.

Steady pressure measurements over the seal flap side-edge in chord-wise direction are shown in Fig. 10 at different flap deflection angles. The distribution shows an overall raise in the suction peak and circulation with the increase in the angle of attack until $\alpha = 28^o$. The suction peak decreased from $\alpha = 28^o$ to $\alpha = 30^o$ and such delayed decrease was associated with the rounded leading-edge format. The suction peak also moved from the pressure side at $\alpha = 0^o$ to the suction side at $\alpha = 5^o$; from $\alpha = 5^o$ it begins to move to the leading-edge. The suction side of the element was affected by a separation that starts at $x/c \approx 0.3$ for high angles of attack. For $\alpha = 30^o$ separation grow and start at $x/c \approx 0.1$.

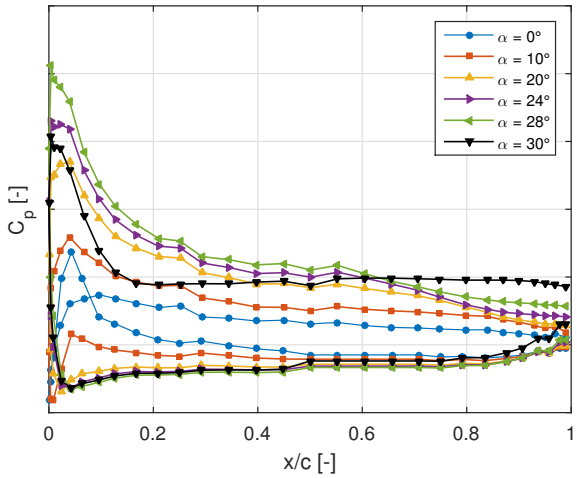

Fig. 10 Pressure distribution over the seal flap side-edge at y/b = 1, M = 0.109 and different angles of attack.

The application of a perforated flap side-edge strongly affects the pressure distribution of the flap. As shown in Fig. 11, for the two perforated side-edge configurations, the suction peak decreased and, consequently, the lift coefficient was affected, which indicates an influence of a perforated tip on the aerodynamic performance. Perforated flap side-edge tips show 10% less flap circulation in comparison with the non-perforated configurations.

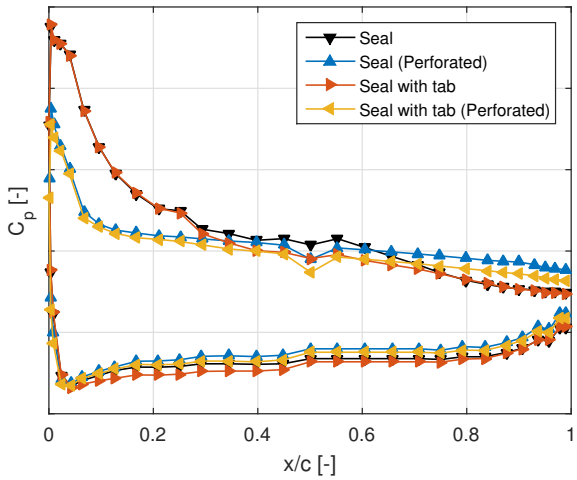

Fig. 11 Effect of perforated tips in pressure distribution at $\alpha = 26^o$ and M = 0.109.

2. Wake Mapping

The wake of the flap model was mapped at several horizontal planes by a 7-hole probe. The three non-dimensional velocity components u^*, v^* and w^* were measured at different constant heights from $Y = -300$ *mm* to $Y = 200$ *mm* (being the flap tip face $Y = 0$ *mm*), 850 *mm* away from the trailing-edge of the model.

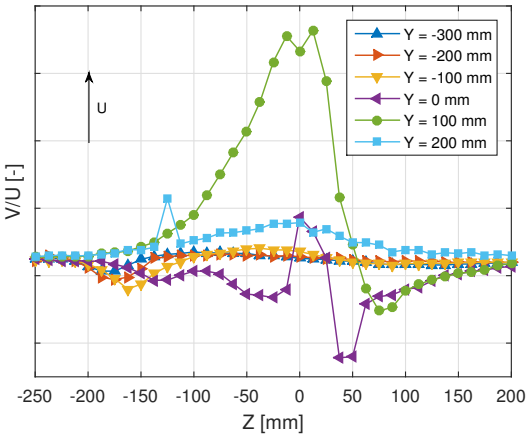

(a) Baseline flap side-edge

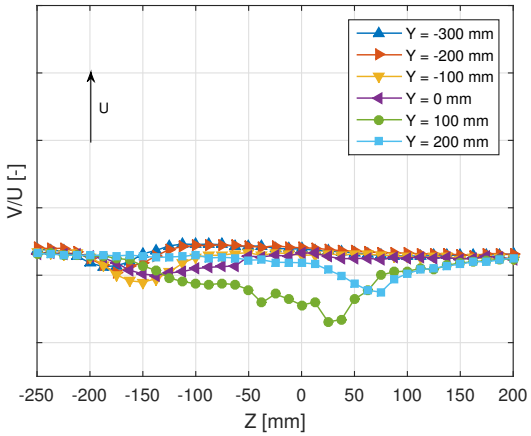

(b) Seal flap side-edge

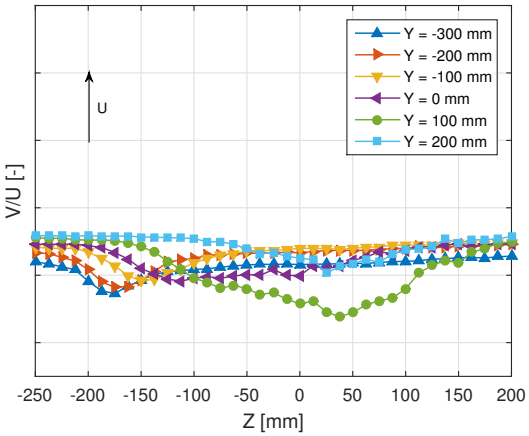

(c) Seal flap side-edge (Perforated)

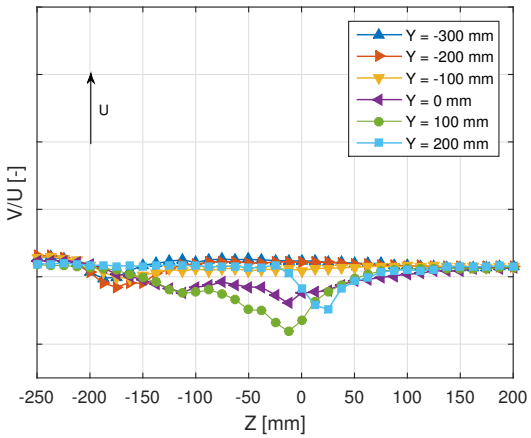

(d) Seal flap side-edge with tab

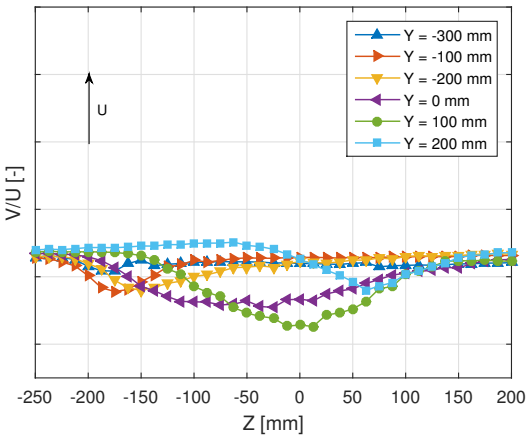

(e) Seal flap side-edge with tab (Perforated)

Fig. 12 Profiles of velocity magnitude in Y axis at α = 5º, M = 0.076 and X = 850 mm.

The most immediate effect of the seal tip configurations was the conversion of the "jet-like" vortex of the baseline flap tip into a "wake-like" vortex, i.e., a vortex core of higher velocity into a vortex core of lower velocity. The plots shown in Fig. 12 contain the profiles of the velocity magnitude for different planes.

In all side-edge configurations from $Y = -300\ mm$ to $Y = 0\ mm$ between $Z = -200\ mm$ and $Z = -100\ mm$, the velocity decrease was related to the wake produced by the trailing-edge of the flap. In the baseline flap side-edge at $Y = 0\ mm$, the vortex exerts an effect that is not present for the other flap tips. For seal tips, the wake profiles show the minimum velocity regions occur behind the trailing-edge of the flap at $Z = 0\ mm$. For such tip configurations, the minimum velocities were displaced to the right in the transition from $Y = 100\ mm$ to $Y = 200\ mm$, which indicates the vortex was shifted resulting from the variations in the tip of the model.

Figure 13 shows the wake profile of velocity v^* and w^* across the vortex core of each configuration. The maximum values were not the same for the negative and positive sides. The asymmetry in the profile is visible for velocity v^* and w^*. Figure 13(a) shows a slower decrease on the right side, whereas such slower decrease is shown on the left side in Fig. 13(b), which corresponds to the areas of lower axial velocity for each velocity component. The perforated tips also displaced the vortex away (up and right to the pressure side) from the flap surface and reduced its intensity.

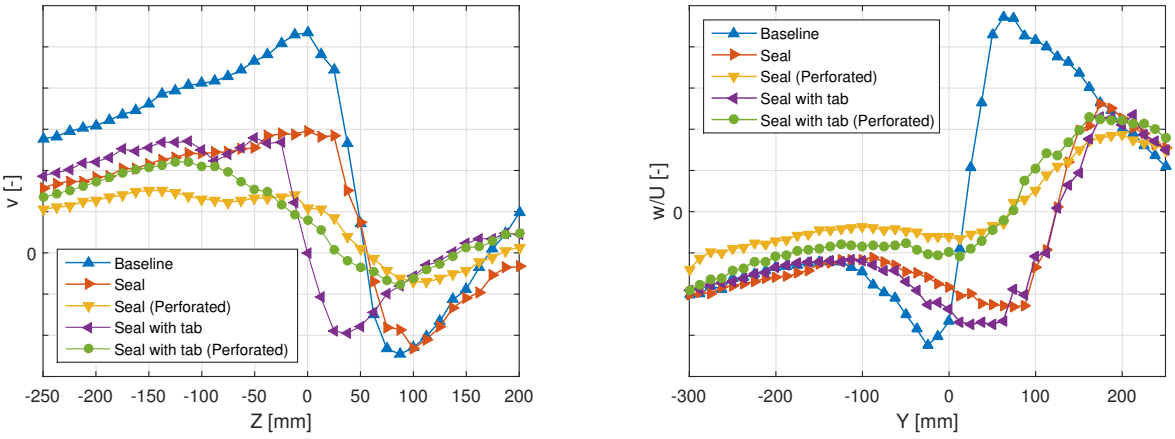

(a) Velocity v^* (b) Velocity w^*

Fig. 13 Profiles of maximum velocity v* in Y axis and maximum velocity w* in Z axis at $\alpha = 5^o$, M = 0.076 and X = 850 mm. For velocity v*: baseline (Y = 25mm), seal (Y = 150mm), seal (perforated) (Y = 100mm), seal with tab (Y = 125mm) and seal with tab (perforated) (Y = 75mm). For velocity w*: Baseline (Z = 50mm), seal (Z = 25mm), seal (perforated) (Z = 25mm), seal with tab (Z = 0mm) and seal with tab (perforated) (Z = 0mm).

Figure 14 shows the 7-hold pitot probe mounted in the traverse system behind the flap model in the wind-tunnel test section.

Fig. 14 7-hold pitot probe behind the flap model.

3. Flow Mapping

A 7-hole probe investigated the flow-field downstream of the flap model. The measurements were taken in a vertical plane, 850 *mm* from the trailing-edge of the model. The axial velocity and vorticity were the most relevant flow measurements in the study of the flow-field. The flow-field maps of velocity u^* and the vorticity are shown in Fig. 15 and Fig. 16, respectively.

The velocity maps for velocity u^* show a region of reduced velocity at approximately $Z = 0$ *mm* position, near the flap side-edge generated by the presence of the vortex. A small region of reduced flow speed downstream the pressure side of the model is probably caused by the presence of the wake formed at the trailing-edge, as shown in Fig. 12. The lowest velocity value reaches approximately $u^* = 0.95$. The velocity maps in Figs. 15(b) to 15(e) revealed the flow was moving up from the tip surface with the use of the seal flap side-edge tips.

Finally, the vorticity mapping indicates the presence of a large vortex downstream the flap tip. As illustrated in Fig. 13, the vortex seems to be weakened for the perforated tips that significantly reduced its intensity. As addressed in the wake mapping analysis, the vortex system was displaced up and right to the pressure side. The maps of the seal side-edge with the tab tip indicate the tab reduced the vorticity movement to the suction side of the flap model.

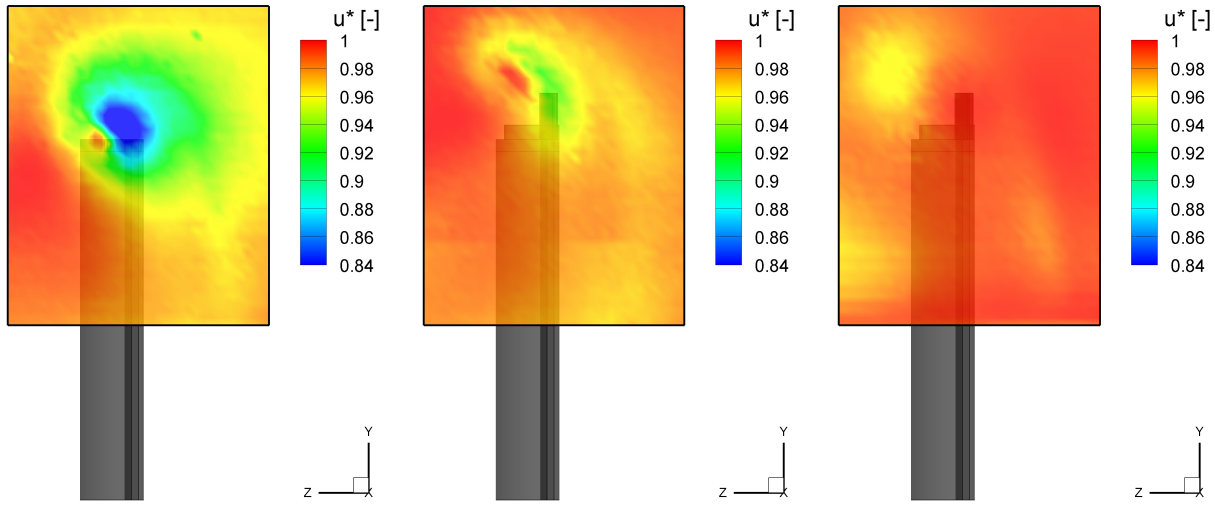

(a) Baseline flap side-edge (b) Seal flap side-edge (c) Seal flap side-edge (Perforated)

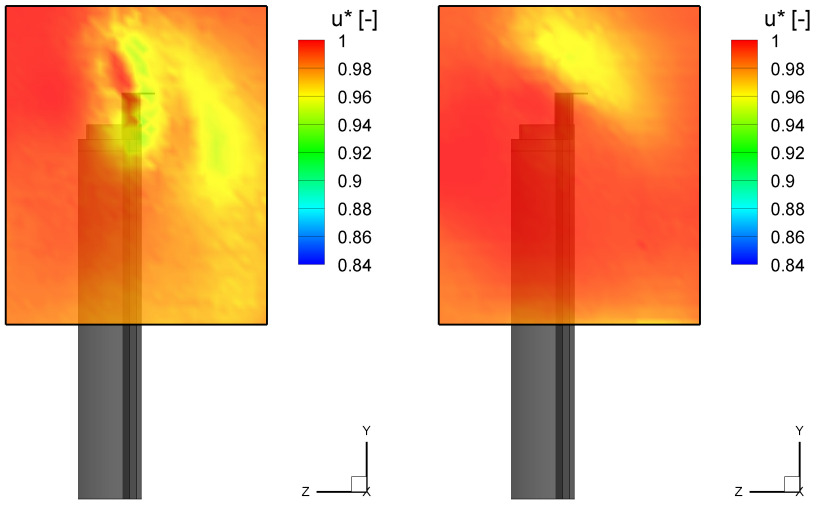

(d) Seal flap side-edge with tab (e) Seal flap side-edge with tab (Perforated)

Fig. 15 Velocity u^* in the X axis at $\alpha = 5^o$, M = 0.076 and X = 850 mm.

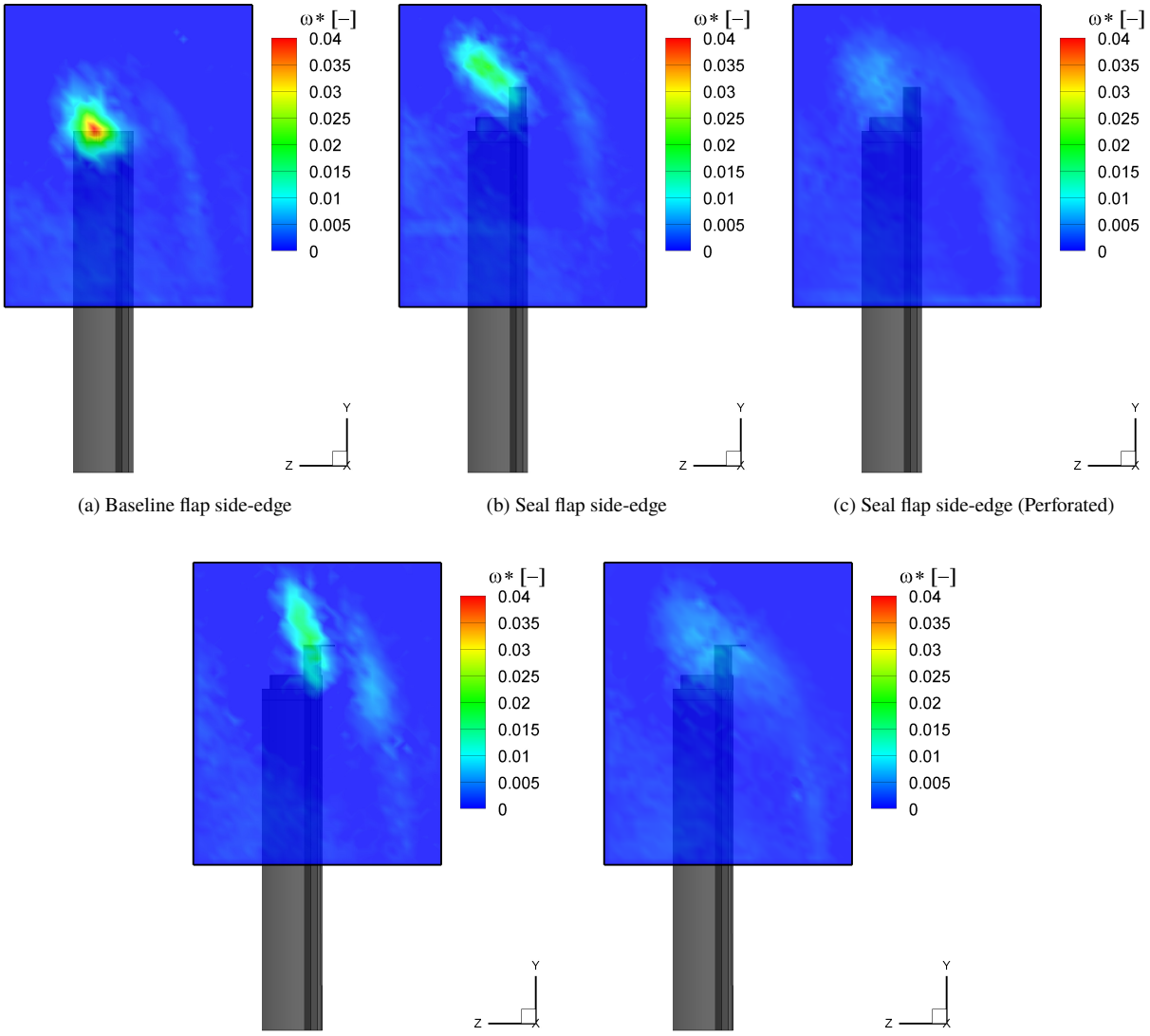

(a) Baseline flap side-edge (b) Seal flap side-edge (c) Seal flap side-edge (Perforated)

(d) Seal flap side-edge with tab (e) Seal flap side-edge with tab (Perforated)

Fig. 16 Vorticity in the X axis at α = 5°, M = 0.076 and X = 850 mm.

4. Flow Visualization

The oil-flow visualization technique was applied at the flap tip surface to investigate the flow behavior around the flap model, particularly, the pathlines and the three-dimensional effects near the flap side-edge. Figure 17 displays the results of the oil-flow visualization for the baseline and perforated flap tips. Additionally, the flow visualizations were analyzed and the flow pattern on the side-edge tips are sketched out. The visualizations clearly show the pathlines created by the primary tip vortex moving from the pressure to the suction side on the tip face. The most visible line is the vortex secondary attachment line induced by the reattachment of the shear layer separated from the pressure side of the flap. The vortex grew in size in the free-stream direction, as indicated by the primary attachment line moving towards the suction surface of the flap side-edge. The results are in agreement with those of Rossignol, K., (2013) [14], who sketched the streamlines of the flow visualization on a flap tip face. The main differences between baseline and seal flap side-edge tips are the recirculation zone produced by the vortex near the pressure side with the presence of the seal and a discontinuity on the leading-edge lines produced by the three-dimensional interaction of the vortex with the turbulence caused by the seal.

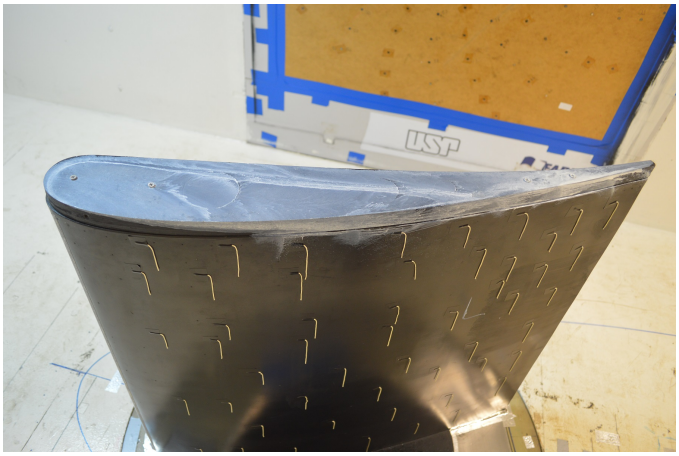

(a) Flow visualization of baseline flap side-edge

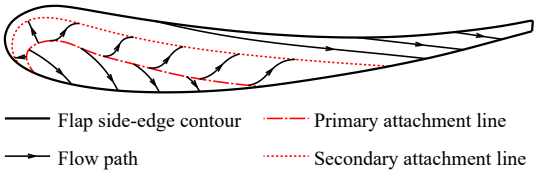

(b) Flow-field sketch of baseline flap side-edge

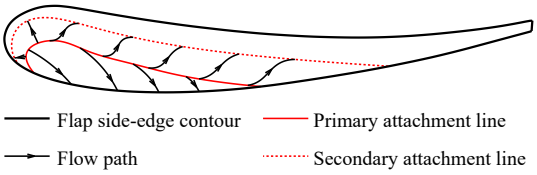

(c) Flow-field sketch of of seal flap side-edge (Perforated)

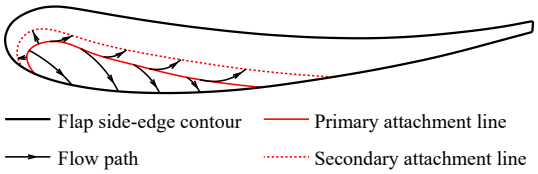

(d) Flow-field sketch of of seal flap side-edge with tab (Perforated)

Fig. 17 Flow visualization and flow-field sketches on the flap tip face at $\alpha = 26^{o}$ and M = 0.076.

B. Far-Field Measurement

1. Background Wind Tunnel Noise

The LAE-1 wind tunnel generates a significant amount of noise itself. The analysis of the background noise aims at assessing its influence on the measurements, regarding spectra, beamforming maps, and Mach scale factor. The sources of wind tunnel background noise are the fan system (the variables that contribute to fan noise are the hub and tip diameter, rotational speed, number of blades and blade-pitch angle), wall boundary layer, test-dependent hardware, and microphone self noise (boundary layer effect over the microphones, screen or cavity perturbations, electronic noise, and free-stream turbulence) [22].

Several measurements were performed for the obtaining of a measure of the background noise observable in the LAE-1 wind-tunnel test section where the phased array microphones are located. Wind tunnel noise was measured for

free-stream velocities of 26, 29, 32, 35 and 38 m/s. The sound pressure levels measured are shown in Fig. 18.

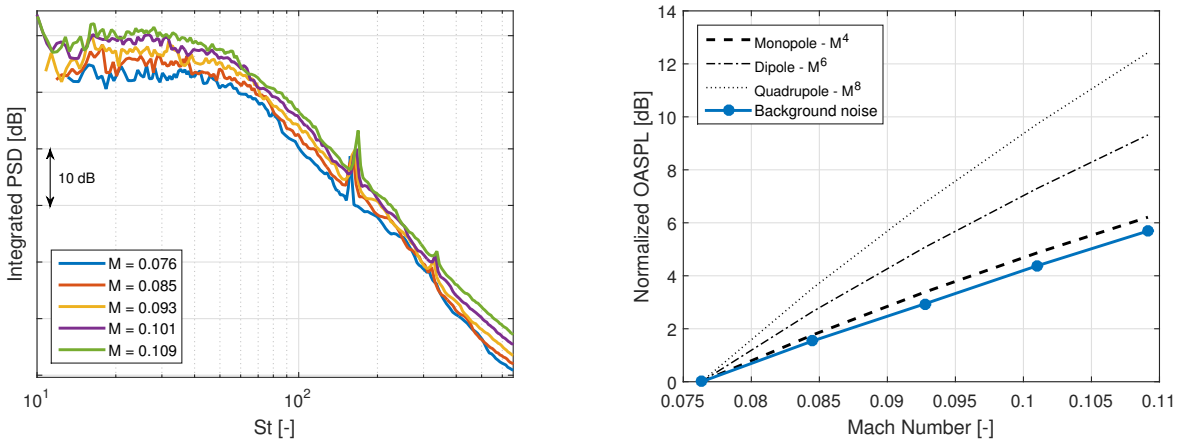

(a) Background noise spectra

(b) OASPL

Fig. 18 LAE-1 background wind tunnel noise.

2. Beamforming Methodology Effects

Besides the Conventional and CLEAN-SC beamforming analyses for all flap tip geometries, DAMAS methodology was also employed for the selected cases. Results for measurements with the three different methodologies are shown in Fig. 19. Broadband noise follows the same shape for all methodologies. Nevertheless, the noise spectra calculated with conventional beamforming and DAMAS methodology preserve the same behavior.

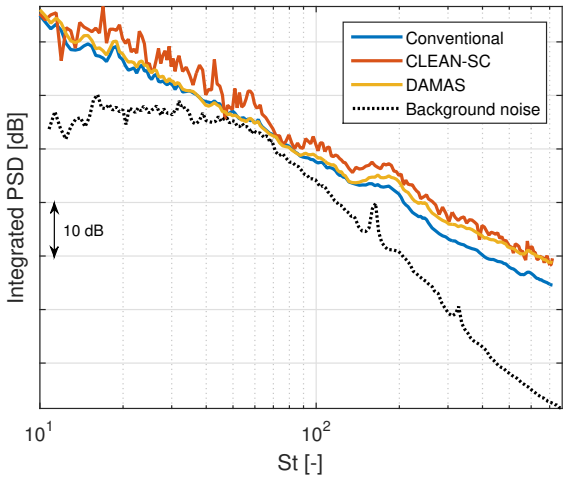

Fig. 19 Effect of the beamforming methodology (Conventional, CLEAN-SC and DAMAS) on the seal flap side-edge tip at $\alpha = 26^o$ and M = 0.109.

The following aeroacoustic results were obtained using conventional beamforming.

3. Beamforming Maps Analysis

Beamforming maps of the three main configurations at $\alpha = 26^o$ and $M = 0.109$ are shown in Fig. 20. The array of microphones evidently identifies a strong noise source from the flap side-edge located at $x/c \approx 0.15$, which corresponds to the first part of the flap side-edge (leading-edge region) local flow-field noise described by Dobrietz, R. and Borchers,

I., (2006) [18]. Noise source maps clearly revealed the way the acoustical radiated noise decreased from low to high frequency spectra.

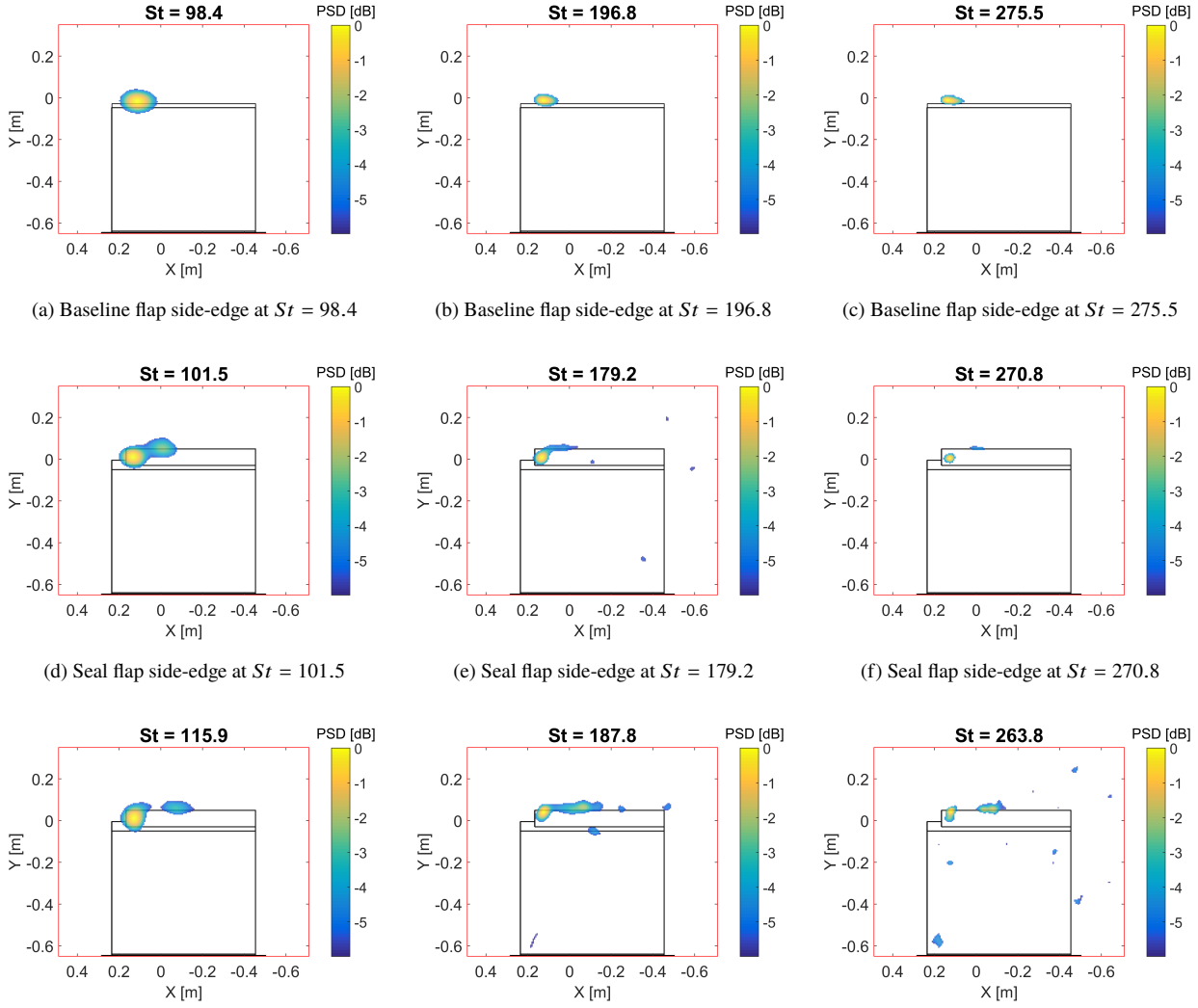

(a) Baseline flap side-edge at $St = 98.4$ (b) Baseline flap side-edge at $St = 196.8$ (c) Baseline flap side-edge at $St = 275.5$

(d) Seal flap side-edge at $St = 101.5$ (e) Seal flap side-edge at $St = 179.2$ (f) Seal flap side-edge at $St = 270.8$

(g) Seal flap side-edge with tab at $St = 115.9$ (h) Seal flap side-edge with tab at $St = 187.8$ (i) Seal flap side-edge with tab at $St = 263.8$

Fig. 20 Beamforming maps of noise source localization at $\alpha = 26^o$ and M = 0.109. The flap model is shown in black and the integration region is shown in red.

4. ROIs Analysis

According to the results in Fig. 21, the predominant noise comes from the side-edge region (ROI 2). The strongest noise level of ROI 2 was produced by the leading-edge region (ROI 3), where the vortex of the turbulent boundary layer on the pressure side moved across the lower flap side-edge. At this point, the vortex was interacting with the surface of the flap side and pressure fluctuations were converted into acoustically radiated noise. Low-frequency noise also was radiated from ROI 4 corresponding to the middle flap side-edge region.

The similarity between the spectra curves does not necessarily mean all different ROIs of the model produce noise in a similar spectrum; it may be related to the integration of side lobes of a higher source in a single place.

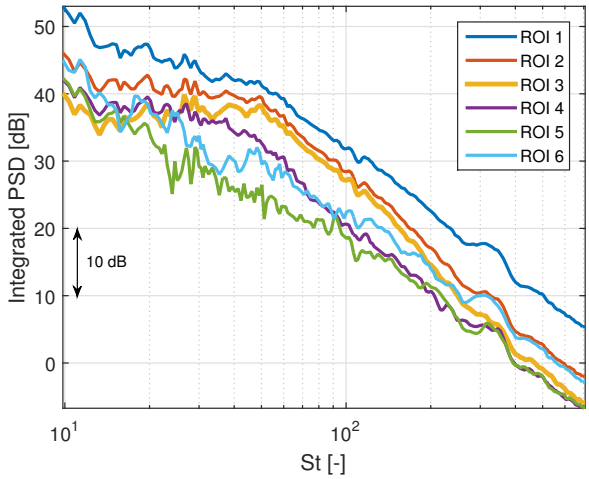

Fig. 21 Effect of ROIs analysis on the acoustic spectrum at α = 26º and M = 0.109.

5. Trip Tape Effects

Acoustic measurements were performed with and without the sand trip tape. Figure 22 shows results of their comparison. No significant differences were observed.

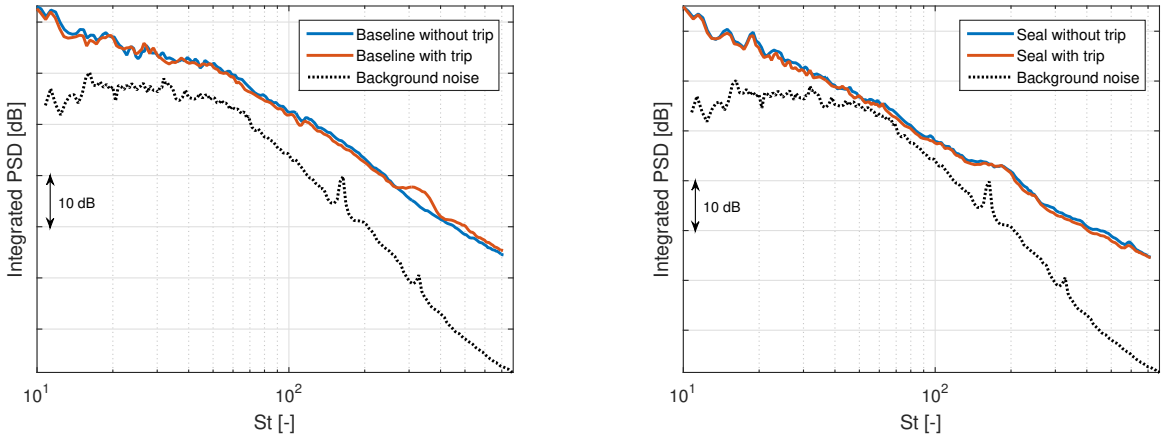

(a) Baseline flap side-edge

(b) Seal flap side-edge

Fig. 22 Effect of trip tape on the acoustic spectrum for the flap model at α = 26º and M = 0.109.

6. Angle of Attack Effects

Figure 23 shows results for the acoustic spectrum variation with six different flap deflection angles for the three main flap tips. For the baseline flap side-edge, small variations were detected for low to mid frequencies; in high frequencies, an increase in the angle of attack caused a small increase in the broadband noise. It was also observed that noise pressure level for seal tips was affected by the higher angles of attack as perceived for $\alpha = 26^o$, 28^o and 30^o. The seal side-edge tips show a greater impact on reducing the vortex at higher angles of attack, which causes the baseline trend to reverse. For such cases, an increase in the angle of attack decreased the spectrum.

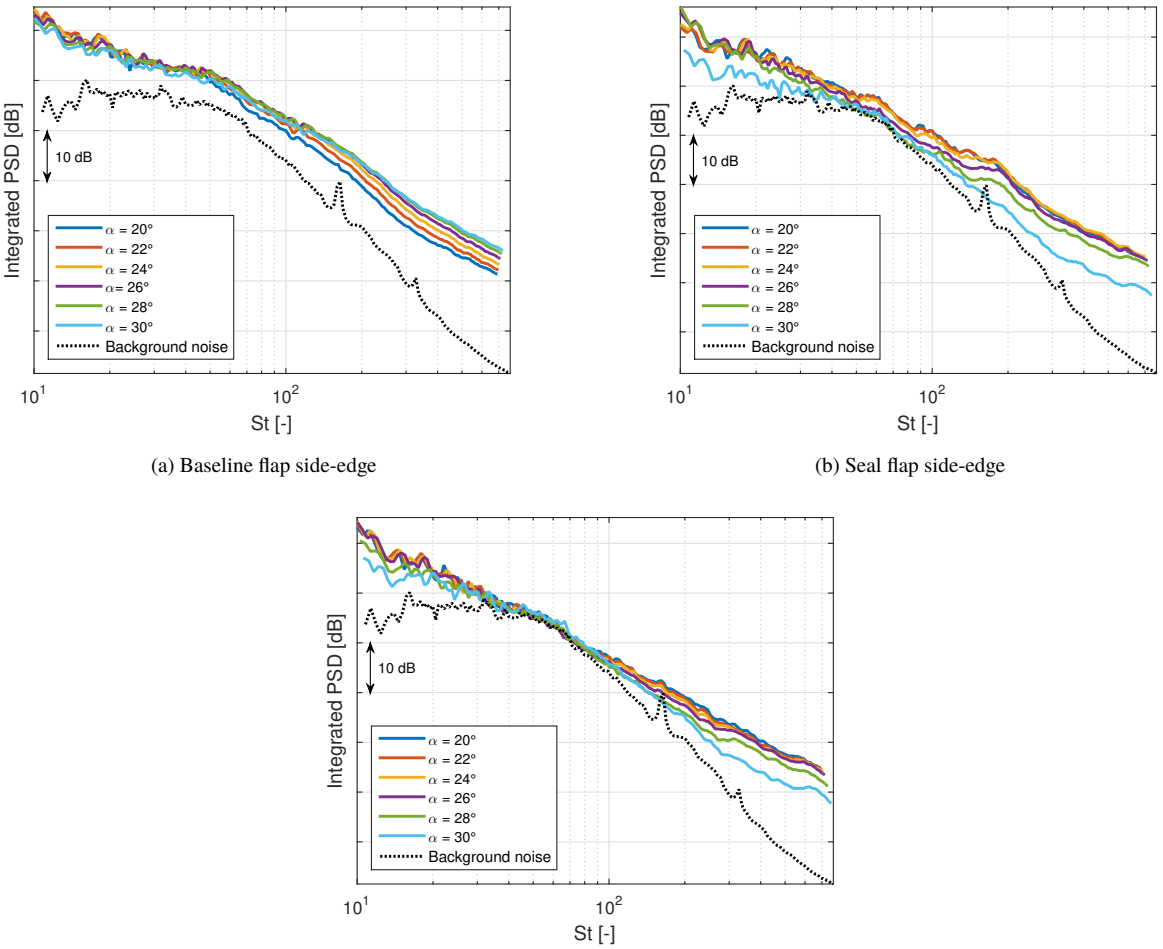

(a) Baseline flap side-edge

(b) Seal flap side-edge

(c) Seal flap side-edge with tab

Fig. 23 Effect of angle of attack on the acoustic spectrum at M = 0.109.

7. Strouhal and Mach Number Scale Effects

Effects of Strouhal and Mach scale are an important issue for the assessment of noise mechanisms for the flap model. An analysis was performed through tests with five different Mach numbers for the evaluation of the effect of the wind tunnel speed variation on the noise produced by the flap model. The results in Figs. 24(a) and 24(b) show the flap noise with baseline tip scales with Strouhal number, whereas with seal tip does not scale.

The Overall Sound Pressure Level progression with the Mach number, shown in Figs. 24(c) and 24(d), clearly demonstrates that scale factor between 6 and 8 is presented. The baseline configuration shows a higher Mach scaling for the Overall Sound Pressure Levels that may be caused by the highest oscillations in low to mid strouhal numbers that increased the overall scale factor locally, as shown in Fig. 24(e).

Figures 24(e) and 24(f) show the way the Mach scale factor changes in function of the strouhal number. A progression is observed between scale with the $4th$ power for low strouhal numbers up to $St \approx 20$ and with $6th$ power. Higher Strouhal number fluctuations were influenced by the shear-layer over the edges of the model for both baseline and seal configurations. The scaling factor is higher than the background noise factor shown in Fig. 18, which indicates the higher the flow speed, the higher the signal to noise ratio (SNR).

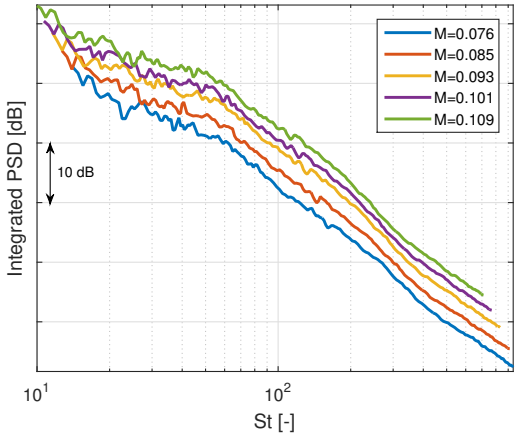

(a) Baseline flap side-edge

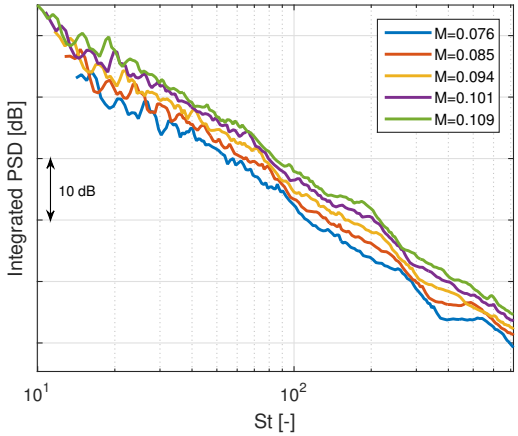

(b) Seal flap side-edge

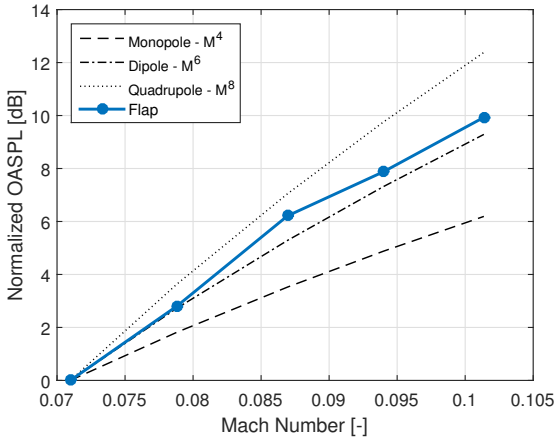

(c) Baseline flap side-edge

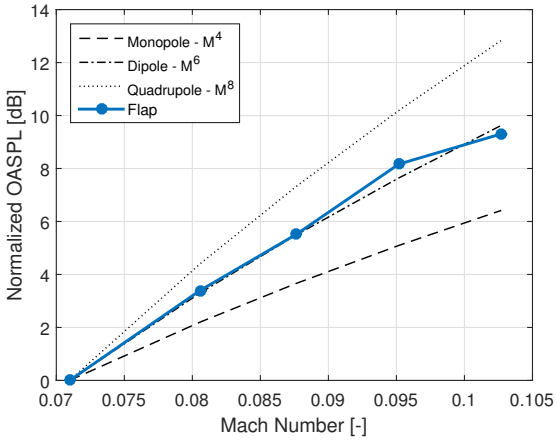

(d) Seal flap side-edge

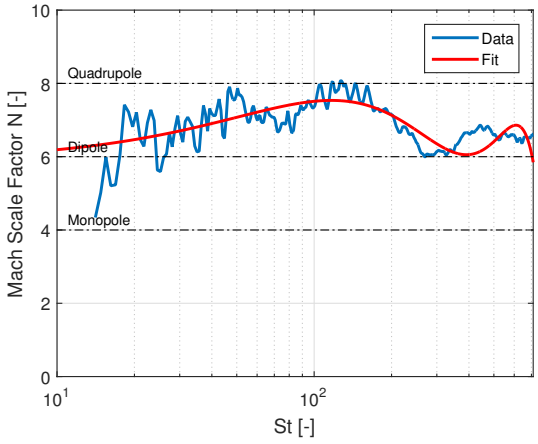

(e) Baseline flap side-edge

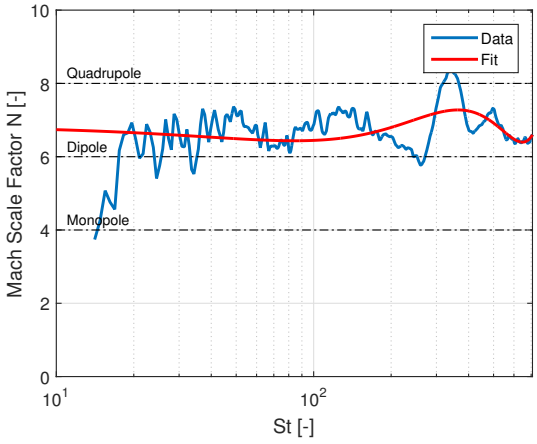

(f) Seal flap side-edge

Fig. 24 Strouhal and Mach Number Scale Effects. Variations in the spectrum with Mach number (a-b), OASPL with Mach number (c-d) and Mach scale factor with strouhal number (e-f) at α = 26º and M = 0.109.

8. Perforation Effects

The comparison in Fig. 25 provides new understanding about the high broadband noise reduction achieved with the use of both seal and seal with tab tips. For non-perforated seal side-edge tips, an important noise reduction in mid to high frequencies was perceived. The tips produced 3.9 *dB* and 6.7 *dB* (Table 2) less noise than the baseline flap side-edge, respectively. Additionally, the effect of the perforation on the tips was also more productive for the seal flap side-edge with 6.1 *dB* (56% less noisy than non-perforated tip) than for the perforated seal with tab flap side-edge with 7.1 *dB* (6% less noisy than non-perforated tip), however, the last configuration was the most efficient flap side-edge tip for noise reduction.

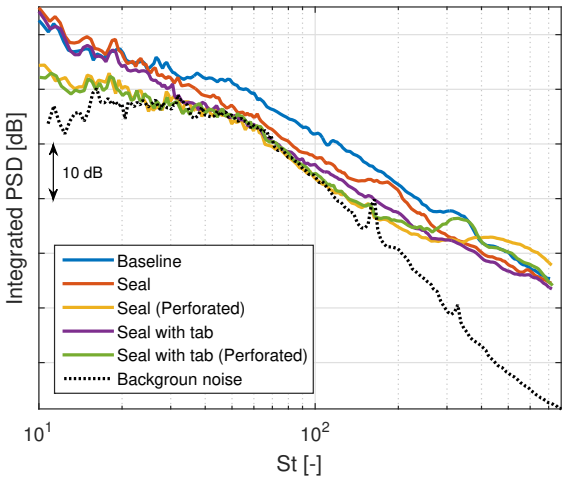

Fig. 25 Effect of perforation on the seal flap side-edge tips at α = 26^o and M = 0.109.

As stated by [8], the slight noise increase in high frequencies for the two tab configurations was associated with the small-scale fluctuations adding to the flow by the tab. The noise spectra increase in perforated tips at high frequencies was related to the sound produced by the perforations at those frequencies.

Table 2 Noise reduction for different flap side-edge tips at α = 26^o and M = 0.109.

Flap side-edge tip	Reduction [dB]
Baseline	0
Seal	3.9
Seal (Perforated)	6.7
Seal with tab	6.1
Seal with tab (Perforated)	7.1

VI. Concluding Remarks

Detailed flow measurements were performed in a large-scale flap model with three main different side-edge tips, in the LAE-1 wind tunnel at the São Carlos School of Engineering - University of São Paulo (EESC-USP), for the evaluation of the noise reduction from flap side-edge. The characteristics of the flow-field in the vicinity of flap tip edges were prominent in relation to the most important sources of airframe aeroacoustic noise. Flap acoustic noise was investigated by a phased array of microphones and beamforming techniques. Steady aerodynamic characterizations were carried out with chord-wise and span-wise pressure measurements distributed along the model and off-surface measurements, by a 7-hole pitot probe. The analyses revealed a clear connection between the far-field noise and the aerodynamic behavior of the vortex system generated at the lower and upper edges of the flap tip.

The aerodynamic flow measurements confirmed the existence of a side-edge vortex which limits aerodynamic performance. The near-field characteristics of the merged vortex were visualized through the oil-flow visualization

technique applied at the flap side-edge face. The aeroacoustic measurements provided information about one of the most dominant source mechanisms of flap side-edge noise. The interaction between the flap pressure side vortex and the side-edge surface plays a major role in noise generation.

In general, the noise spectra of the model are dominated predominantly by a broadband component with no tonal peaks. According to the analysis of the most prominent noise source per ROI, the spectrum results indicated the side-edge region exerts a strong influence on the total noise, which is in agreement with the quantitative beamforming source location maps that showed the main source of noise was located in the leading-edge region. The trip tape used improved the aerodynamic characteristics with a fully developed turbulent boundary layer over the model and no significant effects on the acoustic measurements were observed. Variations in the angle of attack slightly increased the broadband noise at high frequencies for baseline flap tip, whereas seal tips reversed the behavior decreasing acoustic spectrum for higher angles of attack ($\alpha = 26^o$, 28^o and 30^o). Scaling analyses also revealed all tips configurations were consistent with Mach scale factor $N = 6$ corresponding to a dipole noise source.

Modifications to the flap side-edge can essentially reduce the noise radiated from the vortex system. The wake and flow mapping evidenced the behavior of the vortex and the effectiveness of the tested devices to move it and reduced their intensity, which were related to the decrease in noise broadband level. Although seal and seal with tab tips decrease acoustic noise in 3.9 *dB* and 6.1 *dB*, respectively, perforated tips drastically reduce the broadband noise in comparison with the baseline side-edge tip; perforated seal and seal with tab tips reduce 6.7 *dB* and 7.1 *dB*, respectively, of the overall sound pressure level of the flap model. In addition, large-scale perforated noise reduction devices are in agreement with the implementation of real-scale devices without the necessity of scaling tip perforations.

Acknowledgments

The authors acknowledge the financial support from FINEP (Financiadora de Estudos e Projetos), CAPES (Coordenação de Aperfeiçoamento de Pessoal de Nível Superior) and CNPq (Conselho Nacional de Desenvolvimento Científico e Tecnológico).

References

[1] Smith, M. J., *Aircraft noise*, Vol. 3, Cambridge University Press, 1989.

[2] Crighton, D. G., "Aeroacoustics of flight vehicles: Theory and practice. volume 1. noise sources," Tech. rep., NASA Langley Research Center, 1991.

[3] ICAO, I., "Environmental report 2013," *Aviation and climate change*, Vol. 2013.

[4] Dobrzynski, W., "Almost 40 years of airframe noise research: what did we achieve?" *Journal of aircraft*, Vol. 47, No. 2, 2010, pp. 353–367.

[5] EASA, E. A. S. A., "European Aviation Environmental Report," Tech. rep., European Aviation Safety Agency, 2016.

[6] EASA, E. A. S. A., "Validation and improvement of airframe noise prediction tools," Tech. rep., European Aviation Safety Agency EASA, 2012.

[7] Macaraeg, M., "Fundamental investigations of airframe noise," *4th AIAA/CEAS Aeroacoustics Conference*, 1998, p. 2224.

[8] Choudhari, M. M., Lockard, D. P., Macaraeg, M. G., Singer, B. A., Streett, C. L., Neubert, G. R., Stoker, R. W., Underbrink, J. R., Berkman, M. E., and Khorrami, M. R., "Aeroacoustic experiments in the NASA Langley low-turbulence pressure tunnel," .

[9] Dobrzynski, W., "Almost 40 Years of Airframe Noise Research – What did we achieve?" *14th Aeroacoustics Conference*, 2008, p. 37.

[10] Airbus, "Aircraft Noise - Technologies and Operations," Tech. rep., Airbus, 2007.

[11] Herr, M., "Efficient and Airworthy Passive and Active Airframe Noise Control Strategies," *Eingeladener Vortrag im Rahmen der Vorlesungsreihe VKI-Lecture Series Aircraft Noise, von Kármán Institute for Fluid Dynamics, Rhode-St-Genèse, Belgien, 12.–15. März 2012*.

[12] Chow, L. C., Lempereur, P., and Mau, K., "Aircraft airframe noise and installation effects—research studies," *Air & Space Europe*, Vol. 3, No. 1, 1999, pp. 72–75.

[13] Macaraeg, M. G., Lockard, D. P., and Streett, C. L., "In search of the physics: NASA's approach to airframe noise," .

[14] Rossignol, K.-S. S., "Flow field measurements to characterize flap side-edge noise generation," *19th AIAA/CEAS Aeroacoustics Conference*, 2013, p. 2061.

[15] Reichenberger, J., "Noise Control on Flap Side Edge," *INTER-NOISE and NOISE-CON Congress and Conference Proceedings*, Vol. 253, Institute of Noise Control Engineering, 2016, pp. 2424–2428.

[16] Molin, N., Roger, M., and Barre, S., "Prediction of aircraft high-lift device noise using dedicated analytical models," *9th AIAA/CEAS Aeroacoustics Conference and Exhibit*, 2003, p. 3225.

[17] Filippone, A., "Aircraft noise prediction," *Progress in Aerospace Sciences*, Vol. 68, 2014, pp. 27–63.

[18] Drobietz, R., and Borchers, I. U., "Generic wind tunnel study on side edge noise," *27th AIAA Aeroacoustics Conference, Cambridge Massachusetts*, Vol. 2509, 2006.

[19] Catalano, F., "The New Closed Circuit Wind Tunnel of the Aircraft Laboratory of University of Sao Paulo, Brazil," *24TH International Congress of the Aeronautical Sciencies ICAS*, 2004.

[20] Santana, L. D., Carmo, M., Catalano, F. M., and Medeiros, M. A., "The Update of an Aerodynamic Wind-Tunnel for Aeroacoustics Testing," *Journal of Aerospace Technology and Management*, Vol. 6, No. 2, 2014, pp. 111–118.

[21] Fonseca, W. D., Ristow, J. P., Sanches, D. G., and Gerges, S. N., "A different approach to archimedean spiral equation in the development of a high frequency array," Tech. rep., SAE Technical Paper, 2010.

[22] Allen, C. S., Blake, W. K., Dougherty, R. P., Lynch, D., Soderman, P. T., and Underbrink, J. R., *Aeroacoustic measurements*, Springer Science & Business Media, 2013.

[23] Sijtsma, P., "CLEAN based on spatial source coherence," *International journal of aeroacoustics*, Vol. 6, No. 4, 2007, pp. 357–374.

[24] Brooks, T. F., and Humphreys, W. M., "A deconvolution approach for the mapping of acoustic sources (DAMAS) determined from phased microphone arrays," *Journal of Sound and Vibration*, Vol. 294, No. 4-5, 2006, pp. 856–879.